13. Woldemariam, G.A. & Mandal, S.S. Iron(III)-salen damages DNA and induces apoptosis in human cell via mitochondrial pathway. *J Inorg Biochem* **102**, 740-747 (2008).

14. Pradhan, N., *et al.* Induction of apoptosis by Fe(salen)Cl through caspase-dependent pathway specifically in tumor cells. *Cell Biol Int* **38**, 1118-1131 (2014).

15. Drebov, N., *et al.* Ab initio screening methodology applied to the search for new permanent magnetic materials. *New J Phys* **15**, 125023 (2013).

16. S Honary, F.Z. Effect of zeta potential on the properties of nano-drug delivery systems - A review (Part 1). *Trop J Pharm Res* **12**, 265-273 (2013).

17. Jonas, L., Zellmann, E. & Muss, W. Elemental Analysis in Electron Microscopy for Medical Diagnostics. *Microsc Microanal* **13**, 222-223 (2007).

18. Hergt, R., *et al.* Physical limits of hyperthermia using magnetite fine particles. *Magnetics, IEEE Transactions on* **34**, 3745-3754 (1998).

19. Rezaee, M.A., Elahe. Hunting, Darel. Sanche, L´eon DNA-Platinum thin films for use in chemoradiation therapy studies. *Bioinorg Chem Appl* **2012**, 9 (2012).

20. Fukumura, H., *et al.* Effect of ascorbic acid on reactive oxygen species production in chemotherapy and hyperthermia in prostate cancer cells. *J Physiol Sci* **62**, 251-257 (2012).

21. Minai, L., Yeheskely-Hayon, D. & Yelin, D. High levels of reactive oxygen species in gold nanoparticle-targeted cancer cells following femtosecond pulse irradiation. *Sci Rep* **3**, 2146 (2013).

22. Inoue, S. & Kawanishi, S. Hydroxyl radical production and human DNA damage induced by ferric nitrilotriacetate and hydrogen peroxide. *Cancer Res* **47**, 6522-6527 (1987).

23. De Laat, J. & Le, T.G. Effects of chloride ions on the iron(III)-catalyzed decomposition of hydrogen peroxide and on the efficiency of the Fenton-like oxidation process. *Applied Catalysis B: Environmental* **66**, 137-146 (2006).

24. Manda, G., Nechifor, M., T & Neagu, T., M. Reactive oxygen species, cancer and anti-cancer therapies. *Curr Chem Biol* **3**, 342-366 (2009).

25. Bai, J., Rodriguez, A.M., Melendez, J.A. & Cederbaum, A.I. Overexpression of catalase in cytosolic or mitochondrial compartment protects HepG2 cells against oxidative injury. *J Biol Chem* **274**, 26217-26224 (1999).

26. Edulji, S.K. & Nguyen, S.T. Catalytic olefin cyclopropanation using μ-Oxo–bis[(salen)iron(III)] complexes. *Organometallics* **22**, 3374-3381 (2003).

27. Leung, W.-H., Chan, E.Y.Y., Chow, E.K.F., Williams, I.D. & Peng, S.-M. Metal complexes of a chiral quadridentate Schiff base. *J Chem Soc, Dalton Transactions* **7**,

1229-1236 (1996).

28. K.S.Murray. Binuclear oxo-bridged iron(III) complexes. *Coord Chem Rev* **12**, 1-35 (1974).

29. Calderazzo, F., Floriani, C., Henzi, R. & L'Eplattenier, F. Reactions of some metal carbonyls with chelating compounds containing active protons, especially Schiff's bases. *J Chem Soc A: Inorganic, Physical, Theoretical* **(A)**,1378-1386 (1969).

30. Khaliullin, G. & Okamoto, S. Quantum Behavior of orbitals in ferromagnetic titanates: Novel orderings and excitations. *Phys Rev Lett* **89**, 167-201 (2002).

31. Goodenough, J.B. Theory of the role of covalence in the perovskite-type manganites [La, M(II)]MnO_3. *Phys Rev* **100**, 564-573 (1955).

32. Chu, S.H., Singh, D.J., Wang, J., Li, E.P. & Ong, K.P. High optical performance and practicality of active plasmonic devices based on rhombohedral $BiFeO_3$. *Laser Photo Rev* **6**, 684-689 (2012).

33. Segall, M.D., *et al.* First-principles simulation: ideas, illustrations and the CASTEP code. *J Phys: Condensed Matter* **14**, 2717 (2002).

34. Koksharov, Y.A. Magnetism of nanoparticles: Effects of size, shape, and interactions. In: Gubin SP (ed) Magnetic nanoparticles. Vol.6 (ed. Wiley, Weinheim) (197–254) (2009).

35. Yamamoto, T., Takiwaki, H., Arase, S. & Ohshima, H. Derivation and clinical application of special imaging by means of digital cameras and Image J freeware for quantification of erythema and pigmentation. *Skin Res Technol* **14**, 26-34 (2008).

36. Green, A., Martin, N., Pfitzner, J., O'Rourke, M. & Knight, N. Computer image analysis in the diagnosis of melanoma. *J Am Acad Dermatol* **31**, 958-964 (1994).

37. Lopez-Bergami, P.H., *et al.* Rewired ERK-JNK signaling pathways in melanoma. *Cancer Cell* **11**, 447-460 (2007).

38. Bach, D.M., Straseski, J.A. & Clarke, W. Therapeutic drug monitoring in cancer chemotherapy. *Bioanalysis* **2**, 863-879 (2010).

39. Crawford, J.D., Terry, M.E. & Rourke, G.M. Simplification of drug dosage calculation by application of the surface area principle. *Pediatrics* **5**, 783-790 (1950).

40. Pinkel, D. The use of body surface area as a criterion of drug dosage in cancer chemotherapy. *Cancer Res* **18**, 853-856 (1958).

41. Duguet, E., Vasseur, S., Mornet, S. & Devoisselle, J.M. Magnetic nanoparticles and their applications in medicine. *Nanomed* **1**, 157-168 (2006).

42. Weissleder, R. & Pittet, M.J. Imaging in the era of molecular oncology. *Nature* **452**, 580-589 (2008).

43. Lan, G., Wang, Y., Jiang, Y., Zhou, H. & Yi, D. Effects of rare-earth dopants on the

thermally grown Al2O3/Ni(Al) interface: the first-principles prediction. *J Mater Sci* **49**, 2640-2646 (2014).

44. Hirata, K., *et al.* New micro-beam beamline at SPring-8, targeting at protein micro-crystallography. *AIP Conf Proc* **1234**, 863-896 (2010).

45. Otwinowski, Z. & Minor, W. Processing of X-ray diffraction data collected in oscillation mode. in *Methods in Enzymology*, Vol. 276 (ed. Charles W. Carter, Jr.) (307-326) (Academic Press, 1997).

46. Sheldrick, G.M. A short history of SHELX. *Acta Crystallogr Section A* **64**, 112-122 (2008).

47. Ghose, A.K., Viswanadhan, V.N. & Wendoloski, J.J. A knowledge-based approach in designing combinatorial or medicinal chemistry libraries for drug discovery. 1. A qualitative and quantitative characterization of known drug databases. *J Comb Chem* **1**, 55-68 (1999).

48. Marzari, N., Vanderbilt, D. & Payne, M.C. Ensemble density-functional theory for Ab initio molecular dynamics of metals and finite-temperature insulators. *Phys Rev Lett* **79**, 1337-1340 (1997).

49. Sato, I., *et al.* Hyperthermia generated with ferucarbotran (Resovist®) in an alternating magnetic field enhances cisplatin-induced apoptosis of cultured human

oral cancer cells. *J Physiol Sci* **64(3)**, 177-83 (2014).

50. Wu, X., Gong, S., Roy-Burman, P., Lee, P. & Culig, Z. Current mouse and cell models in prostate cancer research. *Endocr Relat Cancer* **20**, R155-R170 (2013).

51. Stecca, B., *et al.* Melanomas require HEDGEHOG-GLI signaling regulated by interactions between GLI1 and the RAS-MEK/AKT pathways. *Proc Natl Acad Sci* **104**, 5895-5900 (2007).

Acknowledgments

We thank K. Otsu, S. Ono, C. Shimada, K. Kezuka, A. Makino, A. Nagasako (Yokohama City University), T. Ohata and K. Akachi (Yokohama National University), and N. Yasuda (JASRI) for their technical assistance.

This work has been supported in part by grants from the Ministry of Health, Labor and Welfare (YI), and the New Energy and Industrial Technology Development Organization (NEDO) (YI), a Grant-in-Aid for Scientific Research on Innovative Areas (22136009) (YI), a grant from the Japanese Ministry of Education, Culture, Sports, Science, and Technology (YI), Next generation Cancer Research Promotion Project of Japan Science and Technology Center (P-direct) (YI), IHI Corporation (HE and YI), and a Grant for Research and Development Project from Yokohama City University (YI). Work at ORNL was supported by the Department of Energy, Materials Sciences and Engineering Division (DJS). Work at RIKEN was supported by the Targeted Proteins Research Program of the Ministry of Education, Culture, Sports, Science and Technology (IH). This work was also supported by a grant for the Platform for Drug Discovery, Informatics, and Structural Life Science from the Ministry of Education, Culture.

Author contribution

H.E. and Y.I. designed the whole study and wrote the manuscript. K.H., M.S. and M.S.Y. conducted X-ray crystallographic study. M.U., R.K., H.F., I.S., M.M.S., T.U., and M.H.S. conducted pharmacological and molecular biological studies. D.J.S. and H.E. conducted the first principle calculation analysis. Y.H., J.H.K. and S.I. conducted chemical studies. J.L. and I.A. conducted MR imaging. M.H.Y. conducted cyclic volutametric study. T.M., N.A., and K.T. conducted magnetic analysis. K.Y. and I.S. conducted transmission electron microscopy (TEM) transmission electron microscopy (TEM) with energy-dispersive X-rays (EDX) studies.

Figures

Figure 1 Anti-cancer effects of salen compounds in cultured cells.

a-f, Effect of various salen compounds on rat prostatic adenocarcinoma cells (MAT-Lu) cells. Cells were cultured in the presence of various salen compounds and analyzed by XTT assays: Cr-salen (**a**), Mn-salen (**b**), cisplatin (**c**), and Fe(Salen) (**d**). (n= 4, $*p<0.05$, $**p<0.01$ vs. control). The induction of apoptosis, evaluated by TUNEL assay, is also shown for Fe(Salen) (n= 10, $**p<0.01$ vs. control) (**e**). DAPI staining for nuclei of non-treated (*Cont*) and Fe(Salen)-treated cells are shown. Immuno-histochemical staining for apoptosis (**f**). *Left;* Cytochrome *c* localization was compared between cytoplasm- and mitochondria-enriched fractions by immunoblotting in the presence or absence of Fe(Salen). Immunohistochemical staining of mitochondria (*red*) and cytochrome c (*green*) is also shown; co-localization is indicated by yellow in the merged images. Note that cytochrome *c* was released into the cytoplasmic fraction in the presence of Fe(Salen). *Right;* Annexin-V binding to the cell surface (*green*). Note that Annexin-V bound to cell membranes only in the presence of Fe(Salen), suggesting induction of apoptosis.

g-l, Effect of Fe(Salen) on various cancer and normal cells. Similarly, cell proliferation was assessed by XTT assays (n= 4, $*p<0.05$, $**p<0.01$ vs. control), and apoptosis by TUNEL assays (n= 10, $**p<0.01$ vs. control). DAPI staining of cancer cells is also shown. The IC_{50} values were approximately 22 μM (clone M3 melanoma cells (**g**), 3 μM (VX2 rabbit squamous cell carcinoma (**h**), and 11.5 μM (POS-1 mouse osteosarcoma (**i**). Fe(Salen) exhibited significant but lower

cytotoxicity towards non-cancer cells, such as human dermal fibroblast cells (NHDF, primary, **j**), rat aortic smooth muscle cells (primary, **k**), and mouse vascular smooth muscle cell lines (Movas, **l**).

Figure 2 Mechanism underlying the anti-cancer effect of Fe(Salen).

a, TEM images of initial (*unsonicated*) and extensively sonicated (6 hours) Fe(Salen) particles (*sonicated*). Extensive sonication at 4°C for 6 hours (Sonifier 250, Branson, 2 kHz) broke up Fe(Salen) particles, as determined by TEM. A scale bar is shown at the bottom. Note that the particle size was reduced, with decreased density, and that the edges of the particles were smoothed compared with those of the unsonicated particles. Unsonicated sample presents sharp and irregular particulate with size of a few hundred nanometers to few micrometers while sonicated particles shows more smoothened and thin morphology. Most likely, sonication destroyed nanoparticles, leading to the reduction of the particles size (see Fig. S4) and their density, and their edges were smoothened. X-ray structural analyses on BL32XU at SPring-8 have revealed that these nanoparticles have a crystalline structure (Fig. 5).

b, Effect of sonication on ROS generation in cell culture. ROS generation was measured in the presence of sonicated Fe(Salen) particles using the fluorescent dye 2',7'-dichlorofluorescein diacetate (DCFH-DA) in MAT-Lu prostate cancer cells (n= 6, NS, not significant, ***$p<0.001$ vs. control).

c, Effect of sonication on ROS generation *in vitro*. ROS generation was compared between unsonicated and sonicated Fe(Salen) particles (6.5 or 25 μM) using the fluorescent dye 2',7'-dichlorofluorescein diacetate (DCFH-DA) in the absence of cells. ROS generation was measured immediately after adding hydrogen peroxide. ROS generation was small with unsonicated Fe(Salen), but substantial with sonicated Fe(Salen); however, this difference was only observed in the presence of hydrogen peroxide. (n= 4, **$p<0.01$ vs. control). **d,** ESR analysis of ROS production. ROS production was evaluated using an EMX-8/2.7 ESR spectrometer (Bruker Biospin, Billerica, MA, USA) with sonicated Fe(Salen). *Control*; 10 μM hydrogen peroxide alone, $H_2O_2(+)$;Fe(Salen)

in the presence of hydrogen peroxide, H_2O_2(-);Fe(Salen) in the absence of hydrogen peroxide. Note that hydrogen peroxide was required to produce ROS.

e, Cytotoxicity. MAT-Lu were incubated with unsonicated or sonicated Fe(Salen) at 37°C for 24 hours. Cell viability was determined by means of XTT assay. (n= 4, *$p<0.05$, **$p<0.01$ vs. control). Note that cytotoxicity was greater with sonicated Fe(Salen) (*lower*).

Figure 3 Magnetic entrapment of Fe(Salen) particles in flowing water.

a, Trapped Fe(Salen) particles in flowing water (also see Movie S1). A permanent bar magnet was placed under a glass tube to trap Fe(Salen) particles in flowing water. Note that Fe(Salen) accumulated more at the edges (*yellow arrows*) than at the center (*white arrow*) of the magnet. Accumulation on the left edge was greater than that on the right because the water flow was from right to left.

b, Calculated magnetic field (magnetic flux density) distribution around the top of the magnet. r and z denote the distance from the magnet axis and the distance from the top of the magnet, respectively.

c, Calculated magnetic force for unit volume of Fe(Salen) or its cluster, for which a spherical shape was assumed. The magnetic force component parallel to the magnet axis (F_z) divided by the volume of the particle (V) is plotted against the distance from the magnet axis (r). d is the distance from the top surface of the magnet. Note that the magnetic force was greatest at the magnet edges (5 mm), where Fe(Salen) was indeed trapped in the flowing water (**a**).

Figure 4 Plots of magnetization versus magnetic field for Fe(Salen) and other salen derivatives.

Magnetization versus magnetic field curve values was generated using a superconducting quantum interference device (SQUID) (Quantum Design MPMS7 system). Each derivative was enclosed in a plastic capsule (Quantum Design) for measurement. The magnetization versus magnetic field curve of Fe(Salen) was plotted from -268°C (5K) to 37°C (310K) (**a**). Changes in magnetization (M/(emu/g)) with applied magnetic field (H/Oe) between -70,000 and 70,000 Oe are shown.

Fe(Salen) particles were stable and retained the same magnetization versus magnetic field curve at 37°C for at least three years in air. *Inset:* Magnified view of changes in magnetization (M/(emu/g)) with applied magnetic field (H/Oe) between -2,000 and 2,000 Oe. (**b**, **c**) Changes in magnetization with applied magnetic field (H/Oe) between 0 and 70,000 Oe are similarly plotted against magnetic field for Cr(II)-salen and Mn(II)-salen at 37°C (310K).

Figure 5 Structure of Fe(Salen).

a.Chemical structure of Fe(Salen).

b. ORTEP. The crystal structure of Fe(Salen). Atomic anisotropic B-factors for non-hydrogen atoms are shown as ellipsoids. Blue, red, purple, and orange atoms represent carbon, oxygen, nitrogen, and iron, respectively. Hydrogen atoms were omitted for clarity. See also Supplementary Movie S3.

c. Projections of the spin-polarized density of states onto Fe *d* orbitals within the LAPW sphere radius of 1.6 bohr. The results of PBE GGA calculations with relaxed atomic positions on a per-atom basis are shown. The majority spin is shown above the axis, and the minority is shown below. Note the broader majority spin features reflecting strong spin-dependent hybridization.

d. Crystallographic data and statistics. For details of data processing and refinement, see METHODS.

Figure 6 Magnet-guided drug delivery in cultured cells and mice.

a-d, Drug delivery in cultured cells. Clone M3 were cultured in the presence of Fe(Salen) (50 μM), and a flat, round magnet was placed beneath the center of the dish for 24 hours. The calculated magnetic force per unit volume of Fe(Salen) or its cluster (assuming a spherical shape) at various distances from the top surface of the magnet was plotted against the distance from the axis of the magnet (**a**). *r* and *z* denote the distance from the magnet axis and the distance from the top of the magnet, respectively. Based on the estimated magnetization of Fe(Salen) particles (0.5 emu/g at 37°C), the magnetic force (F_M) attracting Fe(Salen) was calculated according to the following equation: $F_M = VM_s\, gradH$, where V (m^3), M_s (T) and H (A/m) are the volume of the particle,

saturated magnetization of the particle, and applied magnetic field, respectively. The accumulation of the Fe(Salen) fine particles (**b**) and stained cells (**c**) is shown (*broken semicircle* shows the edge of the magnet). The number of cells was determined at the edge (R1) or at various distances (R2) from the magnet (n= 10, $**p<0.01$) (**d**).

e-i, Drug delivery in mice. Leg tumors were established by grafting MAT-Lu cells into mice. A bar magnet (630 mT, surface magnetic flux density) was used for delivery. Effect of Fe(Salen) with magnet application (**e**). Fe(Salen) (5 mg/kg) (*Fe(Salen)*) was intravenously injected every day in the presence or absence of magnet application for 14 days. Note that the tumor size was decreased when the magnet was applied (*bottom*) compared with when it was not (*upper*), at the same dose of Fe(Salen). Dose-dependent effect of Fe(Salen), 625 μg/kg (**f**) and 5 mg/kg (**g**). *Control,* only saline; *Fe(Salen),* Fe(Salen) without magnet application; *Fe(Salen)+Mag,* Fe(Salen) was administered, and a magnet was applied. (n=4-6 (625 μg/kg) (**f**), or n=7-8 (5 mg/kg) (**g**), $*p<0.05$, $**p<0.01$). Effect of magnet application (**h** and **i**). A magnet was applied for 3 hours every day in the absence of Fe(Salen) for 14 days. Note that magnet application did not affect the tumor growth. (n=2).

Figure 7 Magnet-guided delivery by the sliding method with a stationary magnet.

a-b, The scheme illustrates the sliding method with a stationary magnet (**a**). The magnet was applied to the edge of the expected melanoma growth area for 10 minutes. The magnet was slid by 5 mm along the tail (arrows) and similarly applied for 10 minutes (*upper*). This magnet sliding was repeated 5 times over the length of 30 mm for 3 hours after each injection. Note that the magnet was moved by 5 mm at each sliding because the magnetic field generated by this magnet was strongest within 5 mm of its edge (see Fig.1). Longitudinal sections of mouse tails were chemically stained for Fe(Salen) by Prussian blue (*lower*). Note that the area of Fe(Salen) accumulation is densely stained in blue (30 mm in length), following the magnet-guided drug delivery. *Fe(Salen)+Mag*, Fe(Salen) administration (50 mg/kg/day) with magnet application; *Fe(Salen)*, Fe(Salen) administration without magnet application; *Cont,* saline alone. Effect of magnet sliding by itself (**b**). The sliding of the magnet in the absence of Fe(Salen) (+*Mag*) did not affect melanoma growth. (n=4).

c-f, Effect of magnet-guided drug delivery with the sliding method on mouse tail melanoma model. Melanoma was established in mouse tail. Fe(Salen) (50 mg/kg) was administered intravenously, and a magnet (630 mT) was applied to the melanoma site (also see Fig. 5a and b). This process was repeated for 14 days, and the extension of melanoma pigmentation was evaluated. Comparison of the area of melanoma extension (n=8, $*p<0.05$, $**p<0.01$ vs. control) (**c**). Representative photos of mouse tails with melanoma pigmentation (**d**). Note that mice in the *Fe(Salen)* and *Fe(Salen)+Mag* groups received the same amount of Fe(Salen). Histochemical analysis of melanoma with HE staining (**e**). The broken circle shows the putative area of melanoma. Tissue sections were immunostained with anti-Ki-67 antibody (*Ki-67)* and anti-cyclin D1 antibody (*Cyclin D1*) (**f**). Representative photos are shown. Melanin pigments are shown in brown, and immunopositive signals are shown in blue-black. Note that intensity of both stains was decreased in the *Fe(Salen)+Mag* group. *Fe(Salen),* Fe(Salen) alone; *Fe(Salen)+Mag*, Fe(Salen) with magnet application.

Figure 8 MR imaging of Fe(Salen) *in vitro* and *in vivo* studies.

a-b, MR imaging by sample study. A sample of each concentration of Fe(Salen) particles (0- 1.94 mM) was acquired with a 7-Tesla scanner for T1- and T2-weighted images (**a**). Proton longitudinal (R1) and transverse relaxation rate (R2) of Fe(Salen) were calculated quantitatively (**b**).

c-d, MR imaging *in vivo* study. A schematic figure of magnet application to half of the melanoma tumor is presented (**c**). A permanent magnet (630 mT, surface magnetic flux density) was placed in contact with half of the tumor for 3 hours, and MR imaging was performed. Sagittal slice of T2*-weighted MR images at the tail were obtained (T2*) (**d**). At the Fe(Salen) administration with magnet application (*Fe(Salen) + Mag*), signal reduction at half side of the tumor on T2*-weighted MRI was observed. Representative photos are shown.

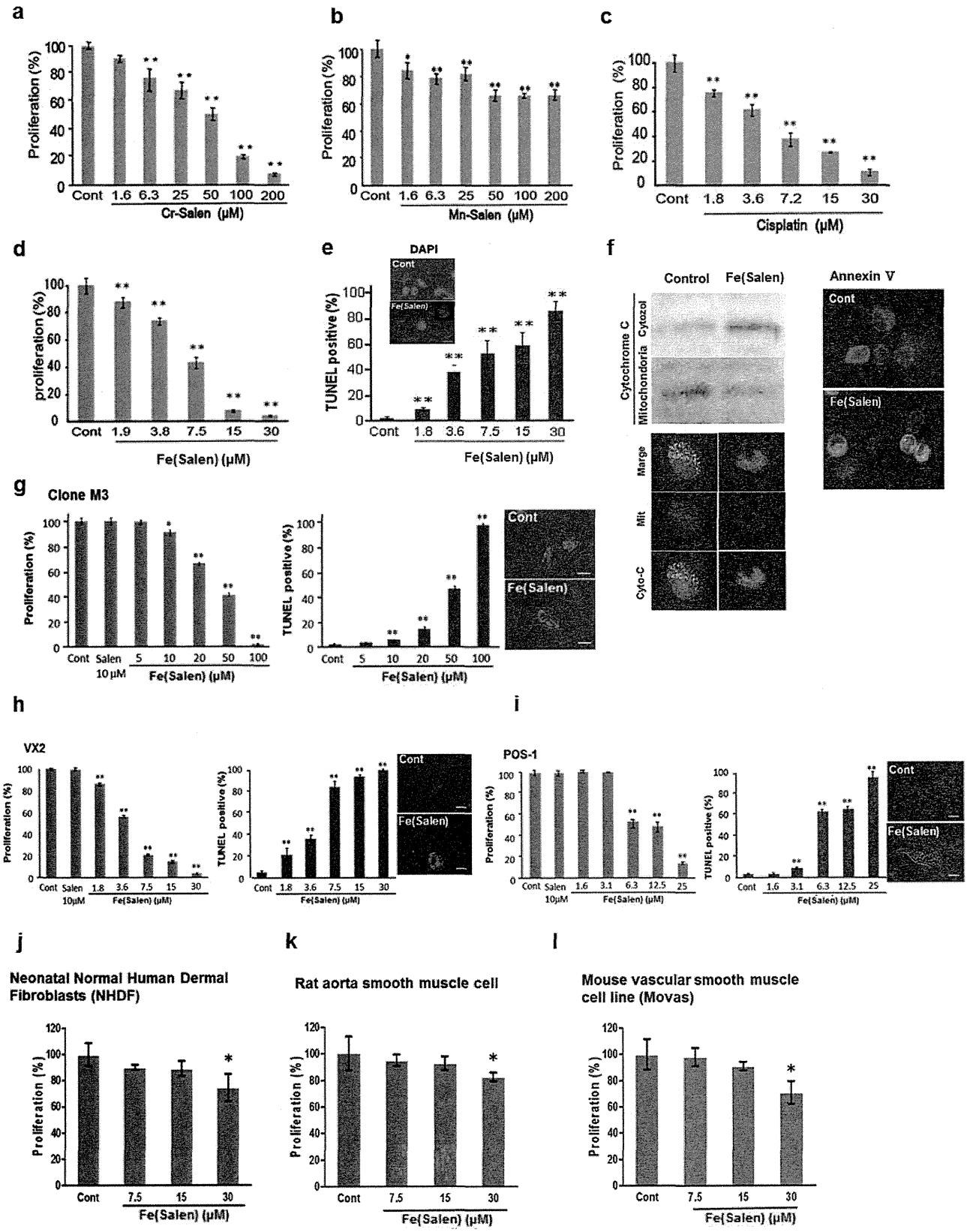
a
Proliferation (%)
Cont 1.6 6.3 25 50 100 200
Cr-Salen (μM)
b
Proliferation (%)
Cont 1.6 6.3 25 50 100 200
Mn-Salen (μM)
c
Proliferation (%)
Cont 1.8 3.6 7.2 15 30
Cisplatin (μM)
d
proliferation (%)
Cont 1.9 3.8 7.5 15 30
Fe(Salen) (μM)
e
DAPI
Cont
Fe(Salen)
TUNEL positive (%)
Cont 1.8 3.6 7.5 15 30
Fe(Salen) (μM)
f
Control
Fe(Salen)
Cytochrome C
Cytozol
Mitochondoria
Marge
Mit
Cyto-C
Annexin V
Cont
Fe(Salen)
g
Clone M3
Proliferation (%)
Cont Salen 10 μM 5 10 20 50 100
Fe(Salen) (μM)
TUNEL positive (%)
Cont 5 10 20 50 100
Fe(Salen) (μM)
Cont
Fe(Salen)
h
VX2
Proliferation (%)
Cont Salen 10μM 1.8 3.6 7.5 15 30
Fe(Salen) (μM)
TUNEL positive (%)
Cont 1.8 3.6 7.5 15 30
Fe(Salen) (μM)
Cont
Fe(Salen)
i
POS-1
Proliferation (%)
Cont Salen 10μM 1.6 3.1 6.3 12.5 25
Fe(Salen) (μM)
TUNEL positive (%)
Cont 1.6 3.1 6.3 12.5 25
Fe(Salen) (μM)
Cont
Fe(Salen)
j
Neonatal Normal Human Dermal Fibroblasts (NHDF)
Proliferation (%)
Cont 7.5 15 30
Fe(Salen) (μM)
k
Rat aorta smooth muscle cell
Proliferation (%)
Cont 7.5 15 30
Fe(Salen) (μM)
l
Mouse vascular smooth muscle cell line (Movas)
Proliferation (%)
Cont 7.5 15 30
Fe(Salen) (μM)

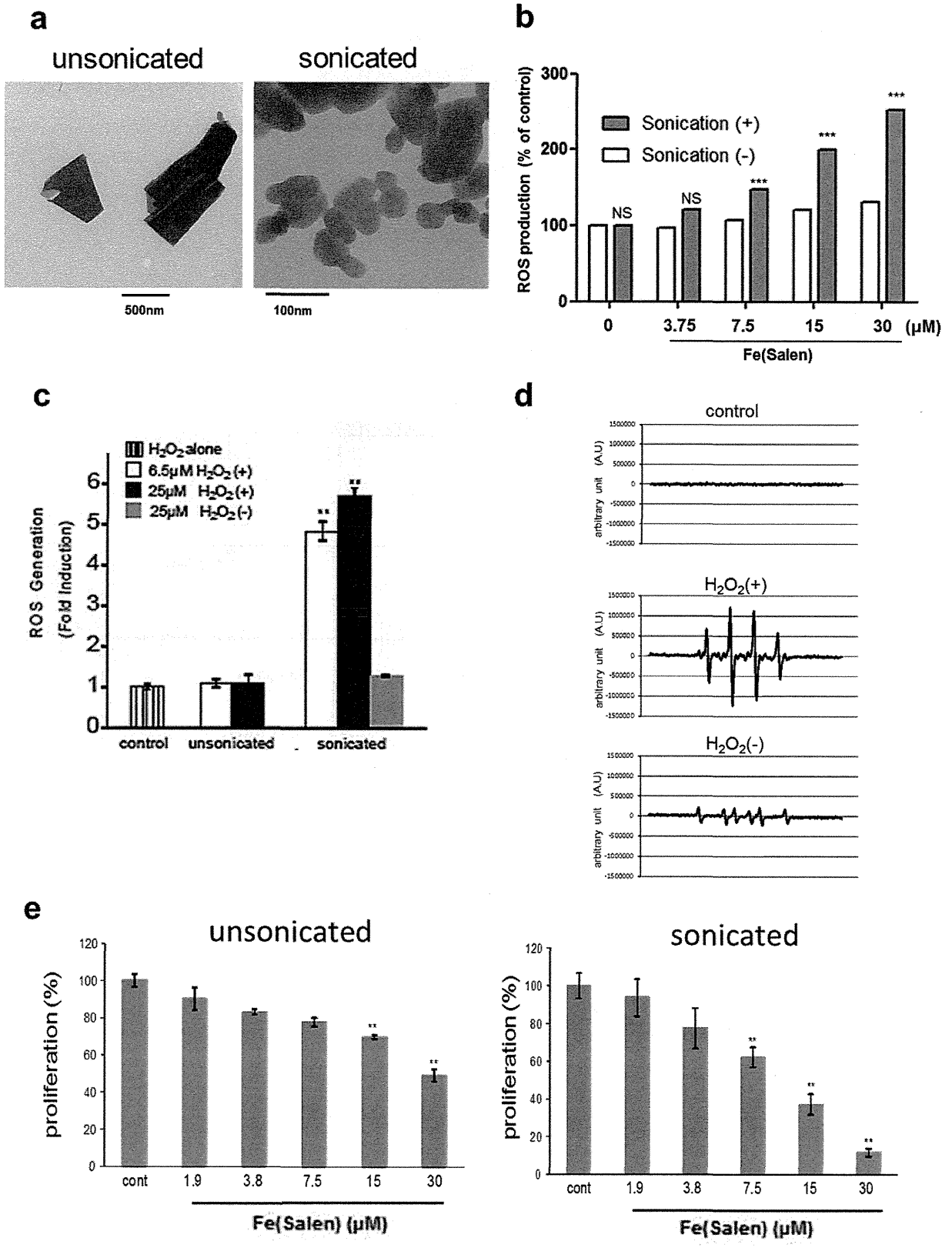
a
unsonicated
sonicated
500nm
100nm
b
ROS production (% of control)
Sonication (+)
Sonication (-)
NS
NS
***
***
***
0
3.75
7.5
15
30 (μM)
Fe(Salen)
c
ROS Generation (Fold Induction)
H2O2 alone
6.5μM H2O2 (+)
25μM H2O2 (+)
25μM H2O2 (-)
control
unsonicated
sonicated
d
control
H2O2(+)
H2O2(-)
arbitrary unit (A.U.)
e
unsonicated
sonicated
proliferation (%)
cont
1.9
3.8
7.5
15
30
Fe(Salen) (μM)

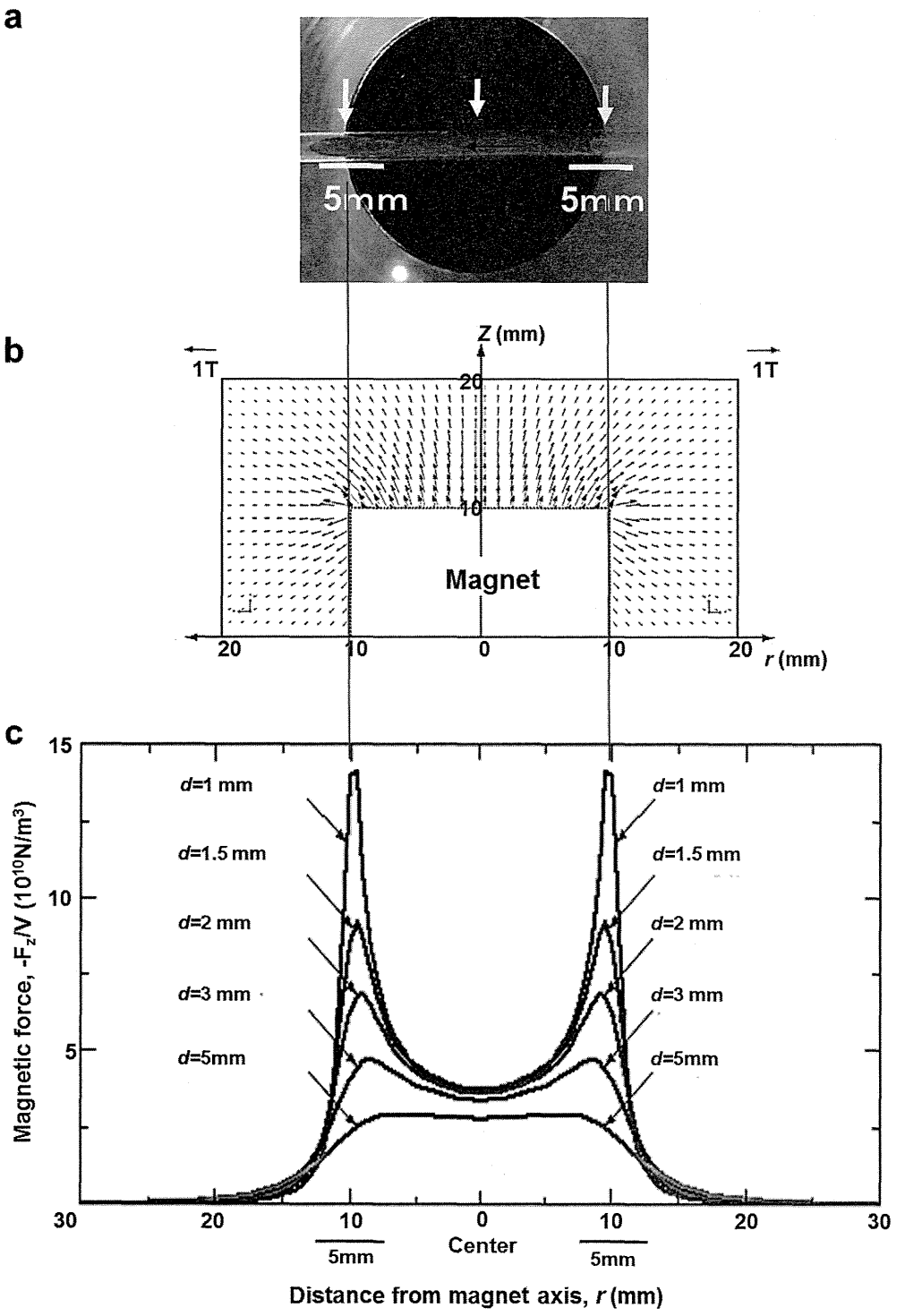
a
5mm
5mm
b
Z (mm)
1T
1T
20
10
Magnet
20
10
0
10
20
r (mm)
c
Magnetic force, -F_z/V (10^10N/m^3)
15
10
5
d=1 mm
d=1.5 mm
d=2 mm
d=3 mm
d=5mm
d=1 mm
d=1.5 mm
d=2 mm
d=3 mm
d=5mm
30
20
10
0
10
20
30
5mm
Center
5mm
Distance from magnet axis, r (mm)

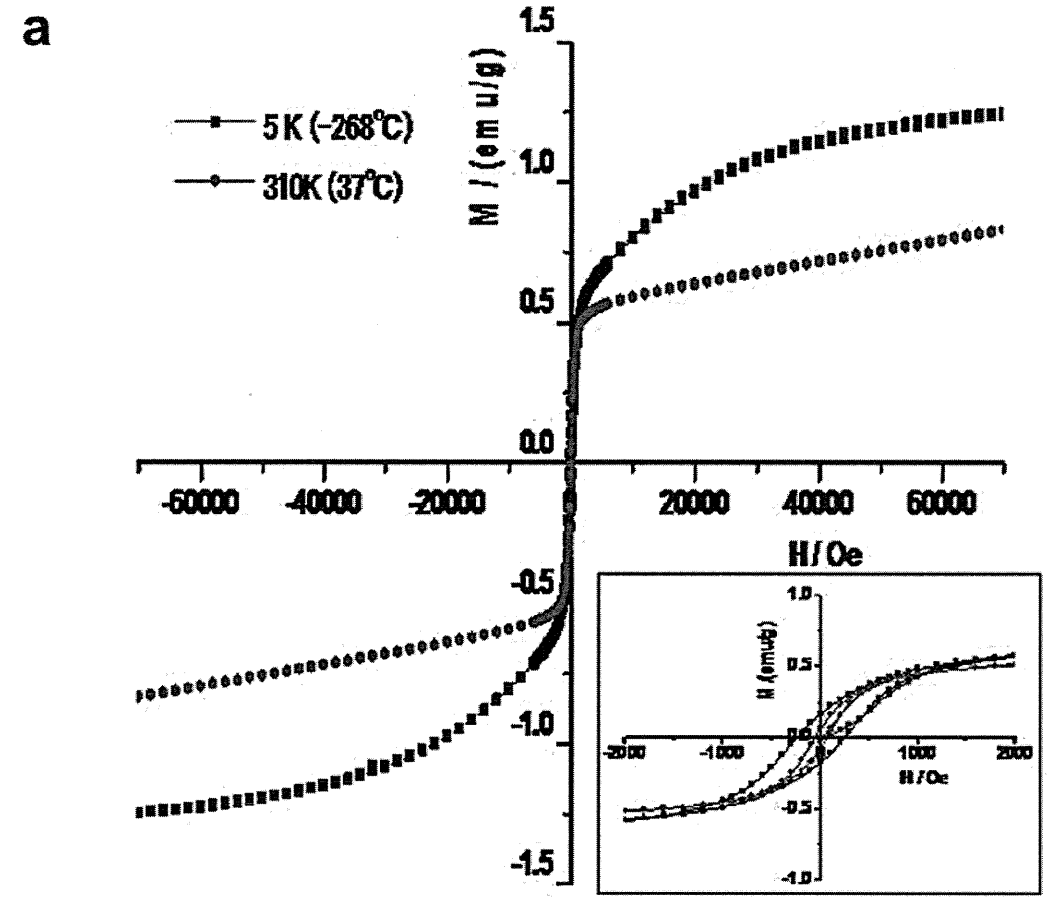
a
5 K (-268°C)
310K (37°C)
M / (emu/g)
H / Oe
1.5
1.0
0.5
0.0
-0.5
-1.0
-1.5
-60000
-40000
-20000
20000
40000
60000
M /(emu/g)
H/Oe
-2000
-1000
1000
2000

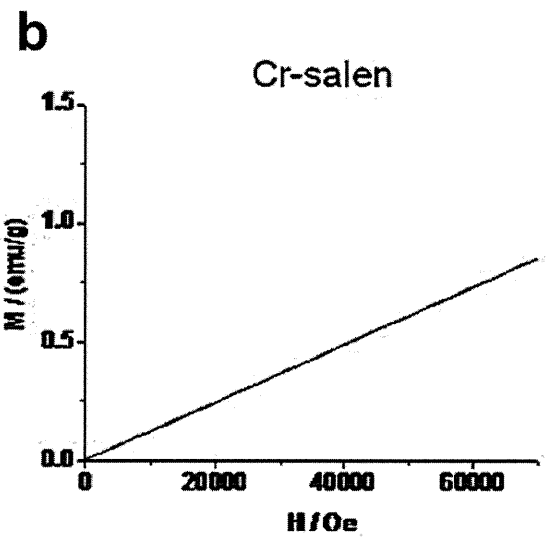
b
Cr-salen
M /(emu/g)
H/Oe
1.5
1.0
0.5
0.0
0
20000
40000
60000

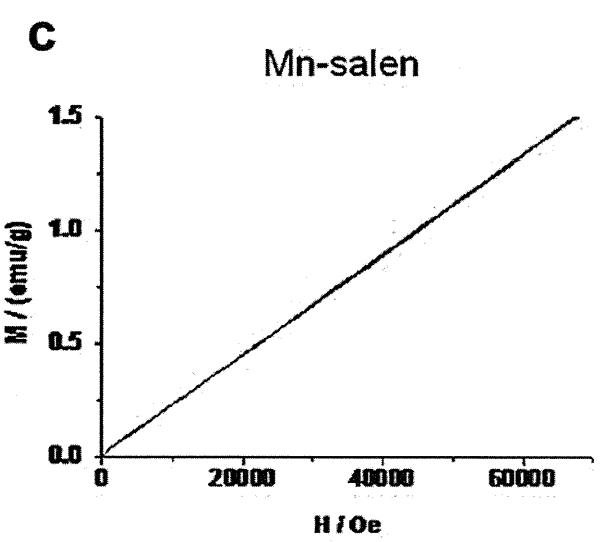
c
Mn-salen
M /(emu/g)
H/Oe
1.5
1.0
0.5
0.0
0
20000
40000
60000

a

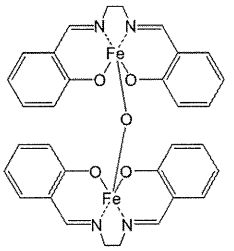

b

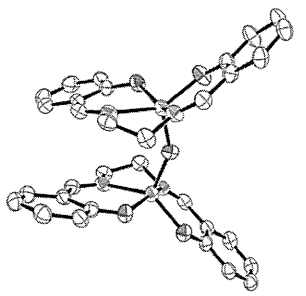

c

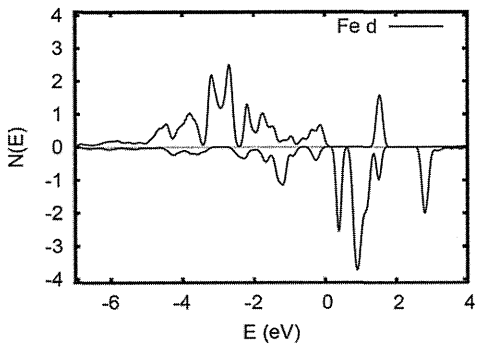

d

Crystal Data	
Compound	$Fe_2C_{32}H_{28}O_5N_4$
Crystal system	Triclinic
Space group	*P*1-
Cell constants with esd's in parentheses	
a, *b*, *c*	10.748(10)Å, 10.76(2) Å, 13.768(10) Å
α, β, γ	66.49(4) °, 81.10(2) °, 73.12(5) °
V	1411.4
Z	2
μ	0.543 mm^{-1}
Data Collection	
Wavelength of X-rays	0.6888 Å
Temperature	100 K
Crystal dimensions	5 × 5 × 40 μm
Beam size at crystal position	1 (horizontal) × 1.5 (vertical) μm
Rotation angle/image	5 deg
Exposure time/image	1 sec
Total no. of images	38
Resolution range	15-0. 87 Å
Refinement Statistics	
Reflections with $I > 4\sigma(I)$	3,236
No. of parameters	429
Weight	$w=1/[\sigma_2(F_o^2)+(0.1000P)^2]$ where $P=(F_o^2+2F_c^2)/3$
Shift/esd	less than 2.089
R_{index}	$R = 0.0800$, $wR2 = 0.1818$
S	1.335
$\Delta\rho_{max}$ and $\Delta\rho_{min}$	0.625 e/Å$_3$ and -0.670 e/Å$_3$

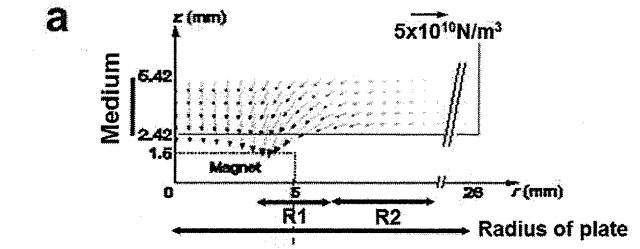

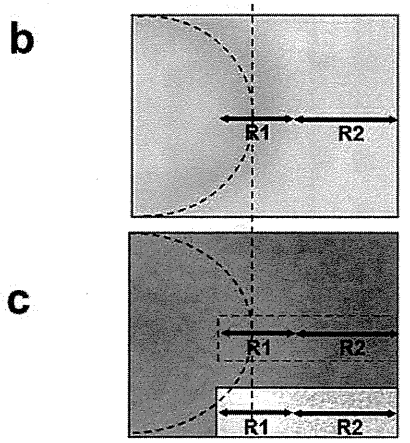

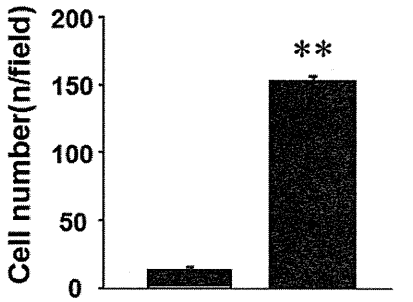

Measurement region	R1	R2
Distance from the center (mm)	3.5-6.5	6.5-12
Magnetic field (mT)	240-80	80-15

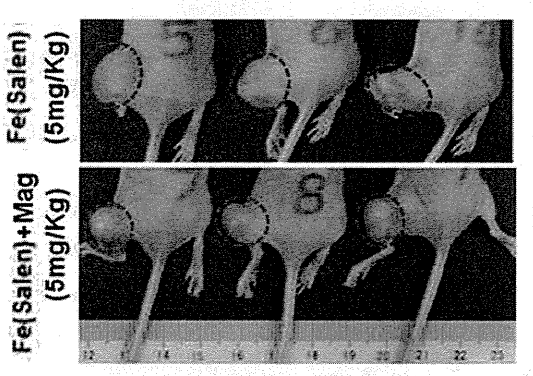

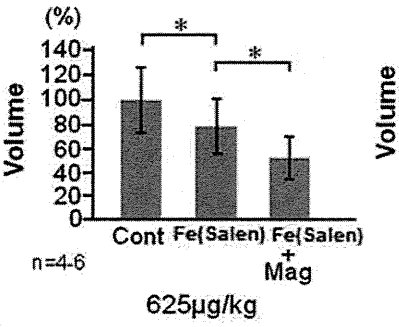

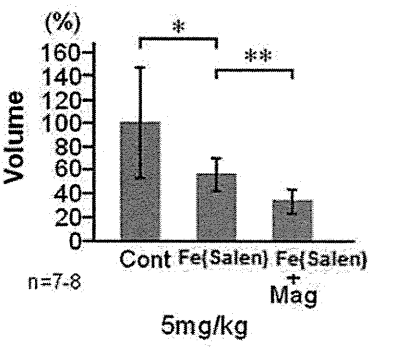

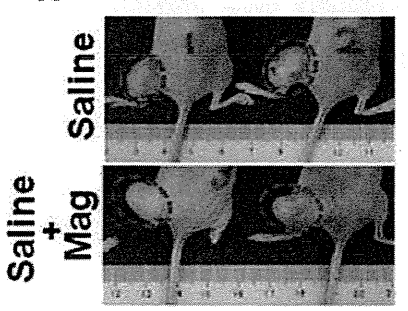

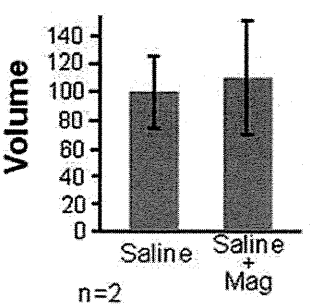

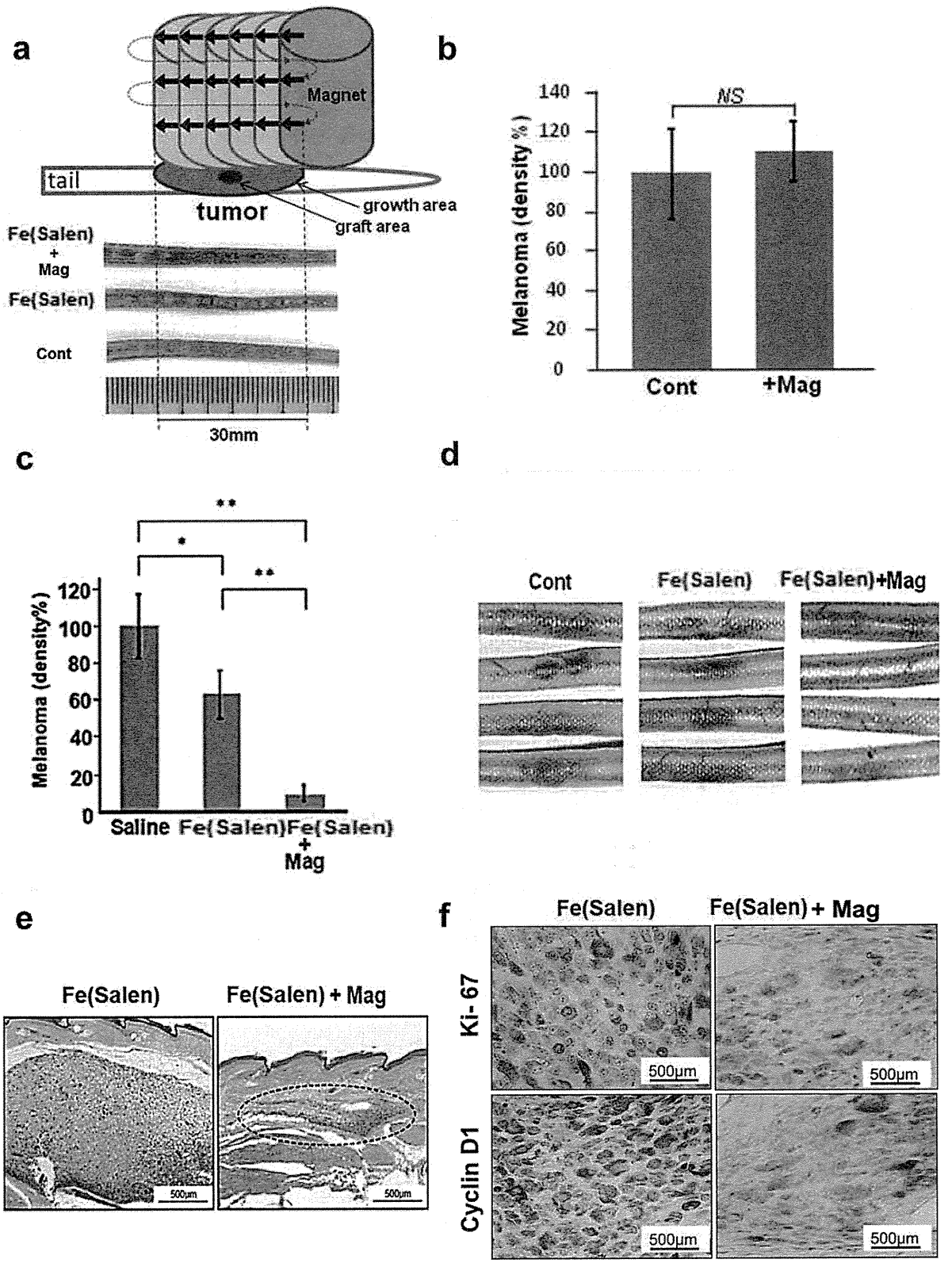
a
Magnet
tail
tumor
growth area
graft area
Fe(Salen) + Mag
Fe(Salen)
Cont
30mm
b
NS
Melanoma (density %)
140
120
100
80
60
40
20
0
Cont
+Mag
c
**
*
**
Melanoma (density%)
120
100
80
60
40
20
0
Saline
Fe(Salen)
Fe(Salen) + Mag
d
Cont
Fe(Salen)
Fe(Salen)+Mag
e
Fe(Salen)
Fe(Salen) + Mag
500μm
500μm
f
Fe(Salen)
Fe(Salen) + Mag
Ki-67
Cyclin D1
500μm
500μm
500μm
500μm

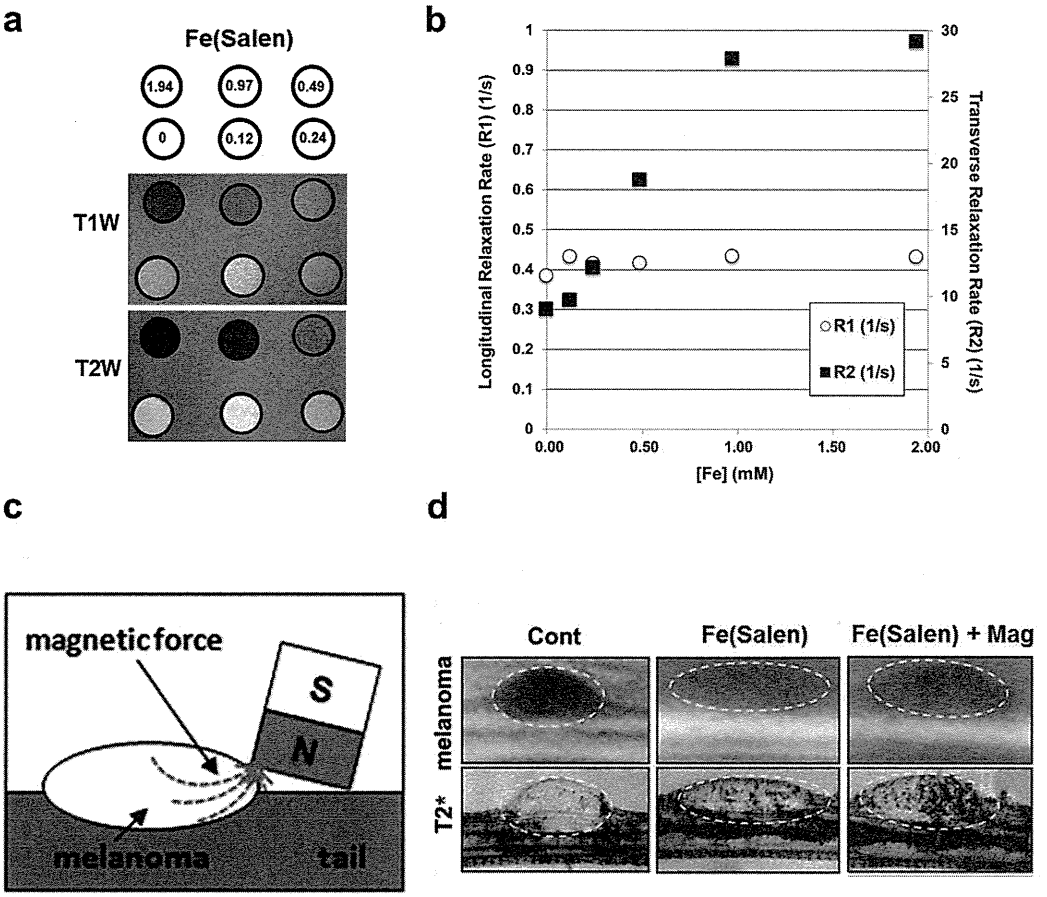
a
Fe(Salen)
1.94
0.97
0.49
0
0.12
0.24
T1W
T2W
b
Longitudinal Relaxation Rate (R1) (1/s)
Transverse Relaxation Rate (R2) (1/s)
[Fe] (mM)
R1 (1/s)
R2 (1/s)
c
magnetic force
S
N
melanoma
tail
d
Cont
Fe(Salen)
Fe(Salen) + Mag
melanoma
T2*